The new DNW-LLF Automotive Test Section

Wilhelmi, H.; Hegen, S.; Melber, S.[1]; Bergmann, A.

German-Dutch Wind Tunnels (DNW)
Voosterweg 31
8316 PR Marknesse
The Netherlands
henning.wilhelmi@dnw.aero
sinus.hegen@dnw.aero
stefan.melber@dlr.de
andreas.bergmann@dnw.aero

Abstract: In recent years, the industrial wind tunnel requirements for automotive tests were largely shaped by the introduction of the Worldwide Harmonized Light Vehicle Test Procedure (WLTP). These regulations posed not only a challenge for existing wind tunnels infrastructures, but also for tests with long vehicles with large frontal surface areas (AF), such as vans or vehicles with box-bodies. The lack of a wind tunnel facility to cover all vehicles sizes in accordance to WLTP motived the German-Dutch Wind Tunnels (DNW) to modernize its Large Low-Speed Facility (LLF). Together with HORIBA an automotive test section (ATS) was developed and build to allow for tests with vehicles from a small form factor up to large, high roofed vans with dual tire configurations at wheelbases of up to 4.7 m and weights of up to 6000 kg. The facility not only allows for aerodynamic tests, but also for the determination of the road loads for energy cycles. In the following sections, the requirements, the development process in CFD and experimental research as well as the first results of the ATS will be presented.

1 Introduction

With the increasing pressure to reduce vehicle emissions (e.g. due EU regulation to combat climate change [1] and customer needs [2]) and to increase their reach, in particular for electrical vehicles, the need to reduce the driving resistances increased. The driving resistance is the sum of three main elements (see also Figure 1):

- The nearly constant rolling resistance,
- The power train resistance, which increases linear with the vehicle speed
- The aerodynamic drag, which increases quadratic with the flow velocity.

[1] German Aerospace Center (DLR), Lilienthalplatz 7, 38108 Braunschweig, Germany

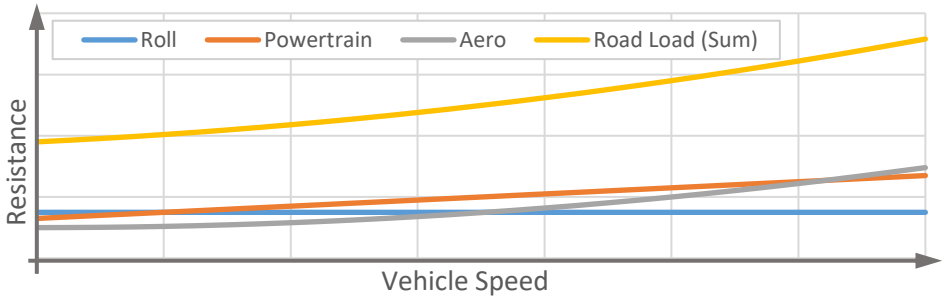

Figure 1: Schematic development of the different resistances with the vehicle speed

These relations indicate that the aerodynamic resistance becomes dominant at higher speeds. According to Hucho [3], the aerodynamic drag equals the roll resistance already at 60 km/h for a Mercedes-Benz B-Class and is almost 5 times the resistance at 120 km/h. Thus, determining the aerodynamic resistance is one of the main factors to determine the economy of a vehicle. However, the other forces – in particular at lower speeds – should not be neglected in the calculations.

To determine the resistances, usually a combination of wind tunnel and roller/flat track test benches or separate coast-down tests are performed. While the coast-down tests allow for determination of all combined forces, this test method lacks in accuracy and repeatability as it is sensitive to weather effects and it can only be conducted late in the development process. Furthermore, it is quite time consuming. Thus, an alternative approach in form of a wind tunnel test combined with roller / flat track tests exists. In an approach for more defined, harmonized testing procedures, a WLTP [4] (for latest iteration) was introduced in 2017. Over the last few years the introduction of the WLTP has led to modernized testing facilities. While most vehicles can be tested in the manufacturer's facilities in accordance to the procedures, in particular larger sized vehicles still provide a significant challenge for wind tunnel tests. The blockage effects are the most prominent challenges, but also the size and range of the wheel drive units (wheel base and track width) as well as the support mechanisms are prominent factors limiting the possible range of vehicles. Thus, there is a need in the market for wind tunnel and rolling resistance tests with larger vehicles as an alternative to the cumbersome coast-down tests.

2 The new automotive test section at DNW LLF

DNW's LLF – due to its large cross-sectional areas of up to 90 m^2 – is able to tests these larger vehicles. In the past, most tests from 1:4 to full-scale automotives and trucks were conducted in closed test sections. While the DNW has experience with moving belt tests, in particular in aeronautical tests, the application of a large, single belt for automotive testing required a high effort at was not feasible for most applications. Thus, most tests were conducted with a static ground in a closed test section. To fill the void of facilities supporting the WLTP certification particularly for larger vehicles – while keeping the blockage effects at a minimum during the measurements – DNW decided to modernize its LLF for automotive tests.

The LLF has various options to change its test section to adapt the system to the customer's request. The options for closed test sections go from a cross-section of

9.5 m by 9.5 m (e.g. for truck tests) over a 8 m by 6 m test sections to a test section with a cross-section of 6 m by 6 m (for tests at up to 465 km/h). The fully open test section has a cross-section of 8 m by 6 m and commonly for acoustic aeronautical tests in an anechoic chamber.

To be in accordance with quasi industry standard of a ¾ open test section, it was decided to develop a modification to the 20 m long, open test section together with HORIBA as supplier of the hardware. The modification consists for a movable test section floor, containing a 5-belt system, an active boundary layer control, a 6-component balance with additional measurement of each wheel force in x-direction as well as a turntable with 12 m diameter (see *Figure 2*). The cross section of the automotive test section (ATS) is 5.9 m by 8 m and thus results in a cross-sectional area of 47.2 m^2. This cross-sectional area results in blockages of around 12 % for vans with high roofs.

Special focus is on the boundary layer treatment for proper ground simulation. The floor length without any extension into the nozzle and collector is 20 m and the width is 14 m with a linear broadening at the aft section to 15 m. It is provided with a scoop, which extends 3 m upstream into the nozzle and a re-entry plate that extends 3 m into the collector. Thus, the total length its about 25 m. The primary boundary layer is removed from the main tunnel flow by the upstream scoop that has a height of 0.08 m with respect to the nozzle floor. Two controllable suction pumps are placed below the tunnel to generate the required volume flow (of up to 42 m^3/s) for different wind speeds. The sucked air can be re-injected into the tunnel flow at the collector or (partly) be released into the tunnel hall.

A secondary boundary layer control system is incorporated in the turntable just ahead of the rolling road. It removes (suction) and reenergizes (blowing), the newly formed boundary layer between primary scoop and the rolling road system. It consists of three independent elements: One system in front of the center belt over its full width of 1.1 m and two systems adjacent to the central device in front of the wheel drive units with a width of 1 m. Each of the three secondary boundary layer control systems is independently controllable

The 5 rolling road belts are made of stainless steel and run at wind tunnel speed up to its maximum of 250 km/h. The standard center belt is 9 m long and 1.1 m wide, while the wheel drive units are typically 0.36 m wide. However, optional a 0.9 m wide center belt is possible. The belts of the wheel drive units are also available in widths 0.28 m and 0.48 m. In combination with wheelbases between 1.9 m and 4.7 m at track widths between 1.43 m to 1.84 m, this allows for a wide range of vehicles from small compact vehicles to long, high roofed vans with twin-tire configurations.

The 6 component balance is integrated in the turntable. The balance rotates around a common vertical axis combined with the turntable. The maximum load range for all components and their accuracy is given in **Fehler! Verweisquelle konnte nicht gefunden werden.**.

Since the test section is around 6 m above the floor of the test hall (see *Figure 2*), the vehicles are loaded via an elevator over a bridge, allowing the next vehicle to be fully prepared in place during a vehicle change.

Table 1: Requested ranges and accuracies for the balance system of the ATS

Component	Range	Accuracy	
F_x	± 6000 N	± 0.015 % FS	± 1.00 N
F_y	± 7500 N	± 0.03 % FS	± 1.25 N
F_z	± 6000 N	± 0.03 % FS	± 1.80 N
M_x	± 7500 Nm	± 0.03 % FS	± 2.25 Nm
M_y	± 7500 Nm	± 0.03 % FS	± 2.25 Nm
M_z	± 5000 Nm	± 0.03 % FS	± 1.80 Nm

Figure 2: View of the ATS in postion in the background with test vehicles in front (courtesy of Volkwagen)

3. Experimental investigations on scale

Exploratory test campaigns were performed in the NLR-AWT (Acoustic Wind Tunnel). For this the overall elements of the ¾ open ATS were duplicated on 1:10 scale. The setup included the tunnel contraction, test floor with primary suction/re-injection and collector. One suction pump (not scaled) was located below the test floor. The suction pump setting was optimized at a wind tunnel reference velocity of 140 km/h by checking on any flow separation on the scoop and the boundary layer development along the test floor.

Several test campaigns were performed with the application of some of the following measurement instrumentation/ equipment:

- Tufts on the test floor to verify whether flow separation occurs at the scoop
- Long static pressure tube at tunnel center-line for axial static pressure development. The tube was supported in the collector and wire suspended to the contraction.
- Pressure taps in the floor from scoop up to the re-entry plate for static pressure distribution on the floor
- Traversing mechanism with pitot-static tube for axial static pressure development at different heights (amongst others 7 cm and tunnel centre) or total pressure tube for boundary layer measurement above the test floor

Fore reference measurements were also performed in the 0.8 m by 0.6 m fully open jet configuration. The tunnel characteristics in terms of axial static pressure C_p distribution (see figure 3) and wind tunnel resonances turned out to be similar to the ¾ open ATS. Also the test floor pressures of the ATS (not shown) collapse with the pressures at tunnel centre line. Tunnel modifications for improvement on the C_p distribution were also investigated. The C_p rise could indeed be delayed with an acceptable penalty of a vertical C_p gradient which does not exist for the standard configuration. However, the methods have not been tested in the LLF yet.

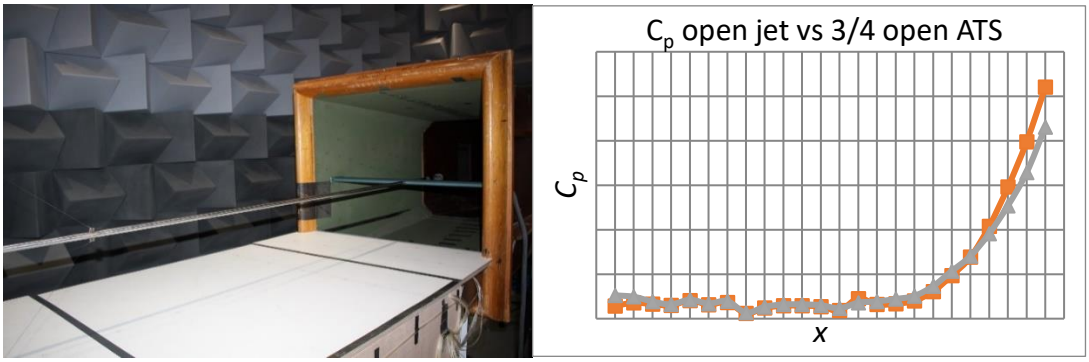

Figure 3: *Long static pressure tube installed in the NLR-AWT (left) and the C_p distributions at tunnel centre line for the open jet (grey) and ¾ open ATS (orange) configurations at reference velocity v = 140 km/h*

The impact of tunnel blockage on the tunnel reference system, as introduced by representative scaled car(s), is investigated by variation of the car distance from the tunnel contraction (distances on scale conformal to car locations in the LLF). At closer car distance the static pressures of the tunnel reference system (located in the contraction end) are clearly disturbed indicating that the plenum method instead of nozzle method should be preferred for determination of the tunnel reference data. Smoke visualizations and C_p distributions behind the car show that the big wake is closed before it enters the collector.

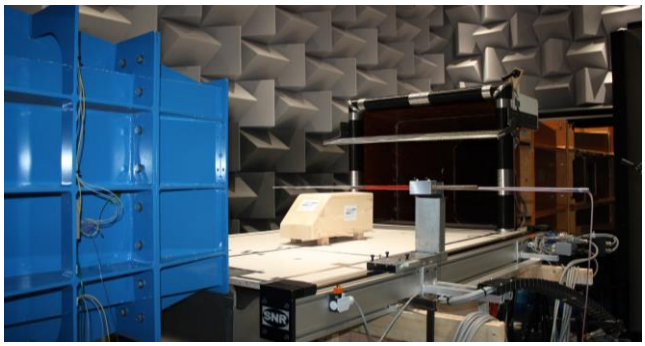

Figure 4: Wooden car model on ATS test floor of the NLR-AWT with pitot-static tube on the traversing mechanism

3 CFD Based Simulation & Optimization

To find the optimal shape and mass flow rates for the boundary layer treatments (in front of the centerbelt and to its sides), numerical flow simulation based on the Reynolds averaged Navier-Stokes equations were used. This was done in a

cooperation between DNW and DLR's institute for Aerodynamics and Flow Technology. The aim is a constant velocity profile in height without crossflow at the center of the belt for the empty test section. For the optimization, a reference velocity of 140 km/h was chosen and the simulation domain consisted of a 2D cut. The domain included the scoop in the nozzle of the wind tunnel (Figure 5 left, green), the suction and blowing re-injection devices itself (right, yellow) and the rolling belt (right, orange; treated by special "moving wall" boundary condition). Based on the optimized geometry found for this reference velocity, the mass flow rates for suction and re-injection at other velocities are optimized in a second step.

The complete shape and mass flow optimization for the center and the side boundary layer treatment systems took place independently, because of different geometrical constraints. This application is based on a numerical optimization chain developed and first applied for the shape optimization of aero acoustic turning vanes in the wind tunnel DNW-NWB [5].

To check the geometry and mass flow rates resulting from the 2D design, the complete center and side parts were simulated in 3D in the next step. With these simulations it can be verified, whether span-wise flow structures over the width, including the outer edges, of the boundary layer control elements occur. Furthermore, possible flow separations in the nozzle/re-injection as well as time depended fluctuations of the flow can be identified. Consequently, the local geometry could be adapted to improve the flow behavior. Though not presented in this paper, the 3D-simulations were also used to identify effects on the pressure distribution of the tunnel with simplified reference configurations as well as with a more detailed model of a car. Finally, these simulations gave a more detailed insight in the flow field and possible optimizations of supply pipes, screens (which are fully resolved in the CFD-Simulations) as well as the feeding of the suction/blowing system.

3.1 Parametric Geometry & Grid Generation

The basis of any kind of optimization is the determination of the free parameters and the parameterization of the geometry. In the case at hand, Figure 5 (right) presents the free parameters in different colours: Red/blue - the mass flow rates of the secondary suction/re-injection, yellow – the inner contours of these elements as well as the shape of the center element.

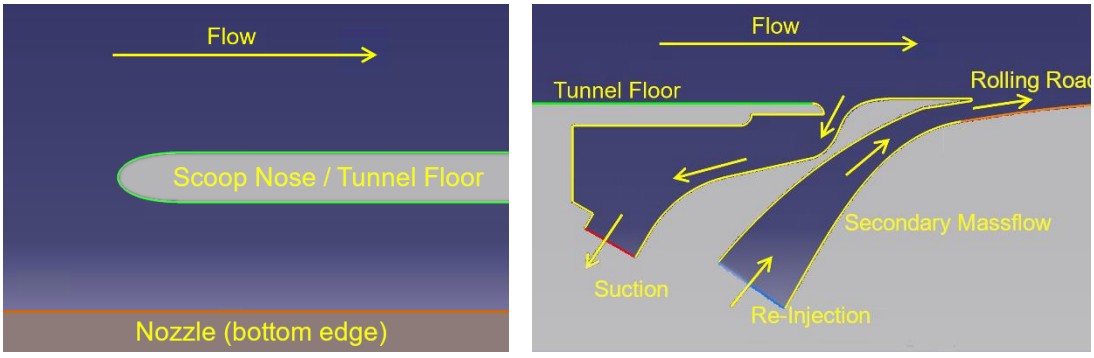

Figure 5: Domain optimizations of primary suction and secondary mass-flow for suction/re-injection

The design was build up as a parametric CAD design. The discretisation of the flow domain in 2D (optimization) and in 3D (verification) took part in the mesh generator SOLAR [6]. It was used due to the overall short runtime and high grid quality. Because topological constraints for 2D meshes in SOLAR the optimization meshes have a finite width of a few cells.

The mesh generator SOLAR consists of a surface mesh generator based on a novel advancing front technique to produce mainly quadrilaterals elements and works on a CAD-patch basis in parametric space. Volume meshing is achieved through a two-stage process. Firstly, the mesh is grown away from the solid surfaces captured in the surface mesh to form a structured mesh of hexahedra for the resolution of the boundary layer. The remaining computational domain is filled with tetrahedral elements in a second step.

A mesh convergence study was performed to minimize the number of grid points on the one hand and on the other the maximize the quality of the flow solution. Overall the mesh results in a n extensive, costly boundary layer discretization and a relatively fine discretization of the suction / re-injection (see Figure 6).

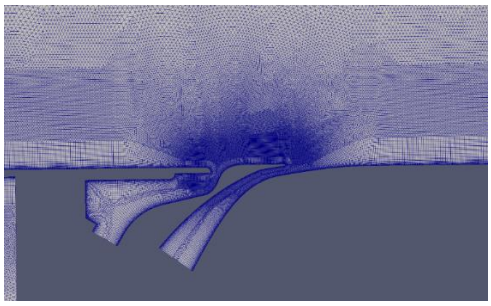

Figure 6: Mesh for optimization in the region of secondary suction / blowing.

3.2 Flow Solver & Optimizer

The solution of the RANS equations is carried out using the hybrid unstructured DLR TAU code [7]. For the closure of the Reynolds-averaged equations the RSM turbulence model [8] is used, which allows for robustness results at a good quality. Due to the low Mach numbers and the resulting stiffness of the RANS equations, low Mach number preconditioning is inevitable. The central JST-scheme in combination with 80% matrix dissipation assures numerical flow solutions with low numerical dissipation. Finally, implicit time-integration is utilized in the TAU code.

The optimization system CHAeOPS (Computational High-Lift Aerodynamics Optimization System) [9] is designed as a modular system. The optimization strategy chosen is the downhill-simplex algorithm SUBPLEX [10]. Previous investigations had shown that the simplex method provides the best compromise of robustness, efficiency and globality when applied to aerodynamic design by RANS simulations. For optimization, the objective function was generated by integrating the (absolute) deviation of the velocity profile at three meters down the second blowing (position of the car bumper) from the reference velocity over a height of 5 meters.

3.3 Results

One distinct result of the optimization runs is the stronger dependence of the resulting velocity profile from the mass flow rates, while the dependence from the geometry itself is smaller. This gives some flexibility for the fine-tuning in the wind tunnel by modifying the suction & blowing rates instead of having to redesign the system.

Another clear result of the optimizations is the centerpiece between the suction and re-injection (which sticks up from the tunnel floor in Figure 7). This fixes the stagnation point of the suction on the rounded nose and reduces the influence of the suction mass flow rate on the resulting velocity profile in front of the car. Other geometries with a bigger nose at a level with the tunnel floor showed a larger movement of the stagnation point at different suction rates and thus, changed the resulting velocity profile.

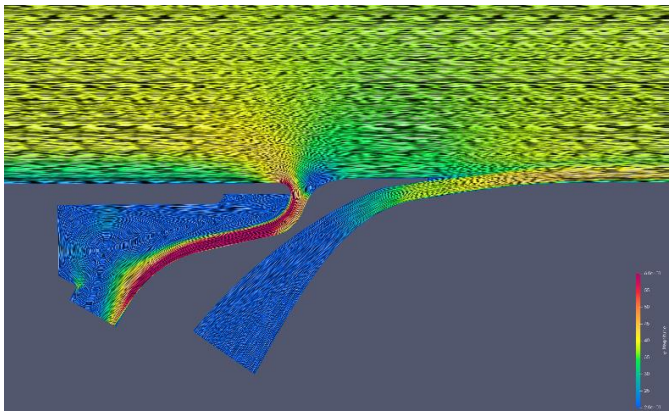

Figure 7: Optimized geometry for center part (absolute velocities and streamlines)

The off-design impact on the boundary layer over the belt was tested with 2D simulations of the optimized geometry by varying the suction- and re-injection mass flows. Overall, changing the suction mass flow has a smaller impact on the velocity profile ("Objective") than varying the mass flow of the re-injection part (Figure 8, left). Further on, in the optimized cases, both mass flows differ by about 10-30 % (with the higher mass flow being at the suction element).

The 3D-simulations show a quite good comparison of mass flow rates in 2D and 3D (determined by the static pressures in the in- and outlet sections). The span wise variation of the flow is quite small even with the split of the center and outer parts.

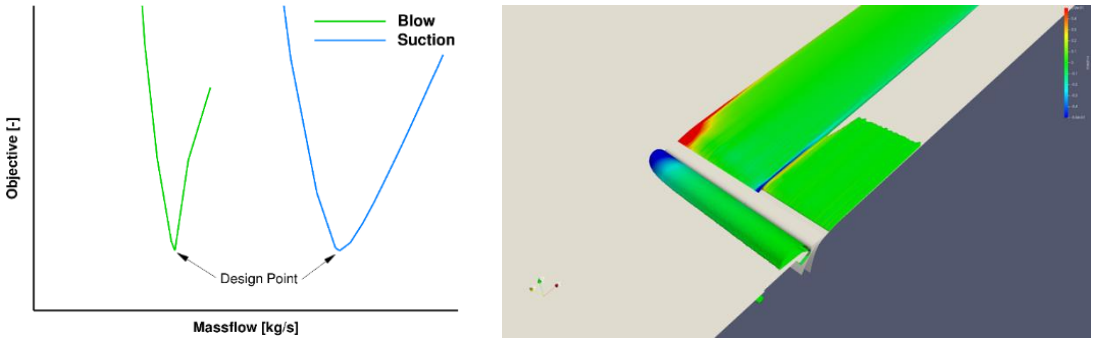

Figure 8: The systems off-design behaviour on the block profile of the boundary layer ("Objective") with varying mass flows at the suction and blowing elements (left) & the iso-contours (39 m/s, span-wise velocity colouring) for a half-model of the suction/blowing in a 3D-simulation (right).

4 WLTP requirement measurements

To show compliance with the WLTP requirements, various tests were conducted. These consisted of aerodynamic tests, belt tests as well as tests of the balance, including measurements with the flat belt system.

4.1 Flow velocities

The flow velocities were measured with pitot static probes in the tunnel centerline (TCL) above the balance center as well as in nine distinct points in the nozzle exit plane (NEP). The nine measurement positions are illustrated in Figure 9. The probe in the tunnel center line was held by 2 symmetric airfoils over the belt. (see Figure 10, left). The measurements in the NEP were conducted with 3 pitot static probes measuring parallel at the 3 required heights (see Figure, right). After each measurement, the system was shifted to a position in the width of the NEP.

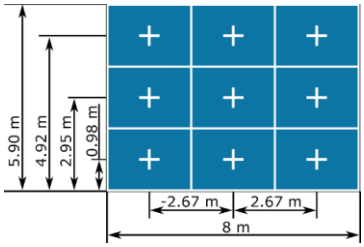

Figure 9: Position of the measurement probes in the NEP

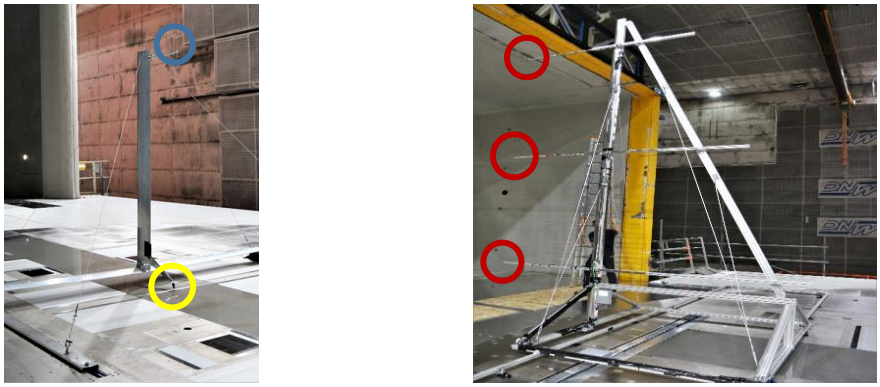

Figure 10: Measurement setup for measurements at the TCL (left, blue circle), at the boundary layer (yellow circle) and at the NEP (right, red circle)

The measurements were conducted with at a targeted air velocity of 140 km/h. In the tunnel centerline the velocity was measured over 600 s (see Figure 11). The velocity was between 139.8 km/h and 140.8 km/h with an average of 140.3 km/h and shows a stable behavior. In the NEP the measurement was over 60 s and averaged at 140.0 km/h over the nine measurement points with a maximum difference of ±0.8 km/h between those points. Both results are well below the WLTP requirements.

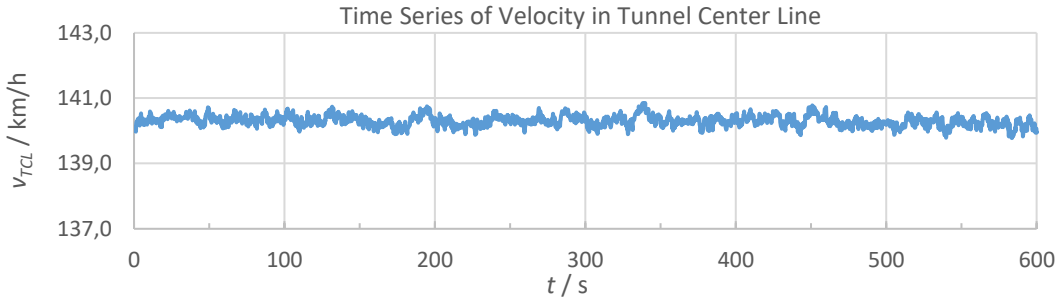

Figure 11: Time resolved velocity data over 10 minutes in the tunnel centerline

4.2 Pressures

Since the pitot static tubes allow for the measurement of the total and static pressures, the previous setups were used for the measure measurements as well (see paragraph 4.1 and Figure 10). In the NEP the standard deviation over all nine measurement points for the total pressure deviation from the mean total pressure divided by the dynamic pressure was determined, while in the TCL the change of the static pressure in form of the pressure coefficient C_p in the region between ±3 m was measured. For the ladder, the holding mechanism for the probe was shifted back and forth in 1 m steps from the balance center and after each shift, the pressure was measured. Since the setup allowed for it, an additional measurement was taken at 4.5 m. The integration time for the measurements was 60 s and the wind tunnel velocity was set to 140 km/h.

The normalized pressures coefficients along the tunnel centerline increase by 0.0056 between -3 m and 3 m, which is well below the WLTP requirement of 0.02. The linearized trend line shows an increase of 0.0007 per meter (see Figure 12). Even when extending the distance to +4.5 m, the linear factor remains at this value. A low crease of the static pressure over a long distance reduced the induced horizontal buoyancy effect during wind tunnel measurements.

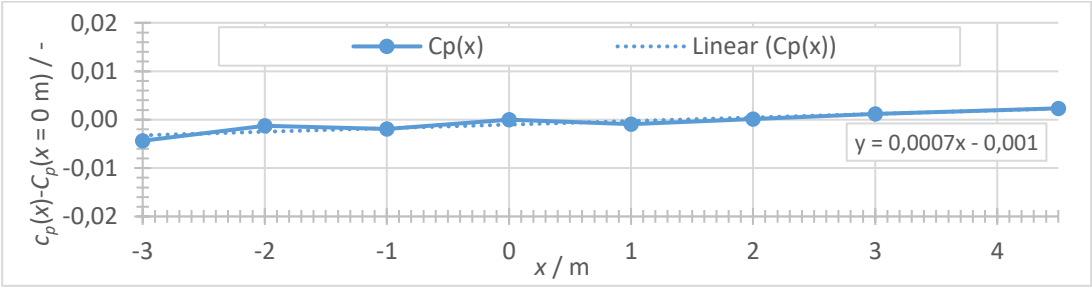

Figure 12: Normalized pressure coefficient distribution along the TCL -3 m to +4.5 m from the balance center in flow direction and the linear trend line with its calculated equation.

The standard deviation of the total pressures in the NEP indicate a slow pressure fluctuation in the NEP of 0.002 or 0.2 % of the dynamic pressure. This also is well within the WLTP requirement of 2 %.

4.3 Turbulence Intensity

The turbulence intensity was measured in the NEP by means of x-wire hot-wire measurements. The holding mechanism was modified for the hot-wires probes in a way that allowed for a 90° turning of the probes to measure the fluctuations in all three flow directions. The data was acquired at 60 kHz over 30 s and an aliasing filter was applied at 30 kHz. In post-processing the data was high pass filtered at 1Hz to prevent non-physical disturbances from entering the turbulent data. Above 3kHz the data is filtered with a linear filter to avoid electrical noise to enter the hotwire data. Additionally a filter was used around 260 Hz to reduce the frequencies by around 3 magnitudes, since mechanical vibrations of the holding system were affecting the results. In particular at the highest positions, mechanical noise, in particular in the y- and z-direction remained an issue, but were too broad to filter out to be separable from the aerodynamic results. The resulting average total turbulence intensities for the wind tunnel at 140 km/h are 0.13 % overall, with 0.05 % in x-, 0.17 % in y- and 0.13 % in z-direction. Despite the mechanical vibrations, this is well below the required 1 % turbulence intensity for WLTP.

With the x-wire hot-wire setup, the flow angles α and β were measured simultaneously. The standard deviation over the nine points was 0.41° and 0.42° respectively. This is also within the regulations.

4.4 Boundary Layer Thickness

The boundary thickness was measured with a boundary layer rake above the center belt in the center of the balance system (see Figure 10, yellow circle). The rake measured the pressures between 16 mm and 66 mm above the moving belt. Due to safety concerns, lower heights were avoided. Together with the aforementioned systems to control the boundary layer thickness (see section 3), the boundary layer at 140 km/h resulted in the distribution presented in Figure 13.

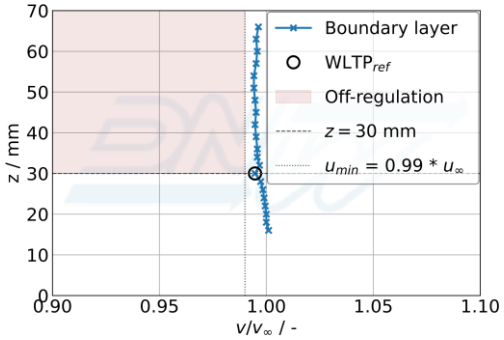

Figure 13: Measured boundary layer with primary and secondary boundary layer treatment in the balance center above the running belt at 140 km/h

The boundary layer at the measured heights is virtually non-existent. The velocities remain above 99% and are within 99.4 % and 100.1 % of the free stream velocity. This is within the requirements of WLTP, which states that the velocities above 30 mm have to be greater than 99 % of the free stream velocity.

5 Summary

The DNW introduced a new automotive test section. Due to the large cross-sectional area of 8 m by 6 m, vehicles ranging from small to long, high roofed vans with wheel bases of up to 4.7 m can be measured with reasonably low blockages. Because of the size, special care was taken in the boundary layer treatment. Its development was supported by detailed CFD simulations from DLR and scaled measurements at NLR.

Furthermore, the test section was setup for WLTP measurements. The aerodynamic requirements are kept and in parts well below the given limits. First commercial tests were conducted successfully in 2023. The full commissioning and certification are projected to be completed by the end of 2023.

6 Bibliography

[1] European Parliament and Council, *REGULATION (EU) 2019/631 OF THE EUROPEAN PARLIAMENT AND OF THE COUNCIL of 17 April 2019 setting CO2 emission performance standards for new passenger cars and for new light commercial vehicles, and repealing Regulations (EC) No 443/2009 and (EU) No 510/201,* Strasbourg: Publication Office of the European Union, 2023.

[2] Aral Aktiengesellschaft - Marktforschung, "Aral Studie - Trends beim Autokauf 2019," Aral Aktiengesellschaft, Bochum, 2019.

[3] Thomas Schütz, Hucho - Aerodynamik des Automobils, 6th ed., Wiesbaden: Springer Vieweg, 2013.

[4] United Nations - Economic and Social Council, World Forum for Harmonization of Vehicle Regulation - ECE/TRANS/WP.29/2020/77, Geneva, Switzerland: United Nations, 2020.

[5] S. Melber-Wilkending and A. Bergmann, "Aeroacoustic opitimization of the NWB airline and turning vanes based on high fidelity CFD and acoustic simulation," in *18th AIAA/CEAS Aeroacoustics Conference*, Colorado Springs, Colorado, USA, 2012.

[6] D. Martineau, S. Stokes, S. Munday, A. Jackson, B. Gribben and N. Verhoeven, "Anisotropic Hybrid Mesh Generation for Industrial RANS Application," in *AIAA 2006-534, 44th AIAA Aerospace Sciences Meeting and Exhibit, 9-12 January*, Reno, Nevada, 2006.

[7] N. Kroll, C.-C. Rossow, D. Schwamborn, K. Becker and G. Heller, "MEGAFLOW - A Numerical Flow Simulation Tool for Transport Aircraft Design," in *23rd ICAS Congress, ICAS 2002, 1.5-10.5.*, Toronto, 2002.

[8] S. Braun, "Implementation of a ln(ω)-based SSG/LRR Reynolds Stress Model into the DLR-TAU Code," Deutsches Zentrum für Luft-und Raumfahrt e.V., 2019.

[9] J. Wild, "Multi objective constraint optimization in aerodynamic design of high lift systems," *International Journal of Computational Fluid Aerodynamics*, vol. 22, no. 3, March 2008.

[10] T. Rowan, "Functional Stability Analysis of Numerical Algorithms.," University of Texas, Austin, Texas, U.S.A., 1990.